
Organized Autotelescopes for Serendipitous Event Survey (OASES): design and performance

Ko ARIMATSU¹

Kohji TSUMURA² **Kohei ICHIKAWA**^{1,3,4} **Fumihiko USUI**⁵ **Takafumi OOTSUBO**⁶

Takayuki KOTANI^{7,1} **Yuki SARUGAKU**⁸ **Takehiko WADA**⁹ **Koichi NAGASE**⁹

&

Jun-ichi WATANABE¹

¹ National Astronomical Observatory of Japan, 2-21-1 Osawa, Mitaka, Tokyo 181-8588, Japan

² Frontier Research Institute for Interdisciplinary Science, Tohoku University, 6-3 Aramaki Aza-Aoba, Aoba-ku, Sendai 980-8578, Japan

³ Department of Physics and Astronomy, University of Texas at San Antonio, One UTSA Circle, San Antonio, TX 78249, USA

⁴ Department of Astronomy, Columbia University, 550 West 120th Street, New York, NY 10027, USA

⁵ Center for Planetary Science, Graduate School of Science, Kobe University, 7-1-48, Minatojima-Minamimachi, Chuo-Ku, Kobe 650-0047, Japan

⁶ Department of Earth Science and Astronomy, The University of Tokyo, 3-8-1 Komaba, Meguro-ku, Tokyo 153-8902, Japan

⁷ Astrobiology Center, 2-21-1 Osawa, Mitaka, Tokyo 181-8588, Japan

⁸ Kiso Observatory, Institute of Astronomy, Graduate School of Science, The University of Tokyo 10762-30, Mitake, Kiso-machi, Kiso-gun, Nagano 397-0101, Japan

⁹ Institute of Space and Aeronautical Science, Japan Aerospace Exploration Agency, 3-1-1

Yoshinodai, Chuo-ku, Sagami-hara, Kanagawa 229-8510, Japan

*E-mail: ko.arimatsu@nao.ac.jp

Received ; Accepted

Abstract

Organized Autotelescopes for Serendipitous Event Survey (OASES) is an optical observation project that aims to detect and investigate stellar occultation events by kilometer-sized trans-Neptunian objects (TNOs). In this project, multiple low-cost observation systems for wide-field and high-speed photometry were developed in order to detect rare and short-timescale stellar occultation events. The observation system consists of commercial off-the-shelf 0.28 m aperture $f/1.58$ optics providing a $2^{\circ}.3 \times 1^{\circ}.8$ field of view. A commercial CMOS camera is coupled to the optics to obtain full-frame imaging with a frame rate greater than 10 Hz. As of September 2016, this project exploits two observation systems, which are installed on Miyako Island, Okinawa, Japan. Recent improvements in CMOS technology in terms of high-speed imaging and low readout noise mean that the observation systems are capable of monitoring ~ 2000 stars in the Galactic plane simultaneously with magnitudes down to $V \sim 13.0$, providing $\sim 20\%$ photometric precision in light curves with a sampling cadence of 15.4 Hz. This number of monitored stars is larger than for any other existing instruments for coordinated occultation surveys. In addition, a precise time synchronization method needed for simultaneous occultation detection is developed using faint meteors. The two OASES observation systems are executing coordinated monitoring observations of a dense stellar field in order to detect occultations by kilometer-sized TNOs for the first time.

Key words: Kuiper belt: general – Kuiper belt: observations – instrumentation: detectors – methods: observational – occultations

1 Introduction

More than 10^{11} kilometer-sized (hereafter km-sized, with radius $r \sim 1 - 10$ km) trans-Neptunian objects (TNOs) are thought to lie in the Kuiper belt and beyond, i.e., the scattered disk (Duncan & Levison 1997; Volk & Malhotra 2008), and the Oort cloud (Oort 1950). The TNOs are thought to be remnants of icy planetesimals and thus are of key importance for the study of the early phase of the outer solar system. Recent collisional-evolution models by Schlichting et al. (2013) have shown

that the size distribution of the present Kuiper-belt objects still contains the signatures of the size distribution of the planetesimals. Since the planetesimal size before runaway growth is one of the major open issues for planet formation theories (Chiang & Youdin 2010), the size distributions of km-sized TNOs would thus give fundamental knowledge about the accretion processes from the early stages of the solar system. In addition, determining the present size distribution of the km-sized TNOs will provide the information on the present-day impact and cratering rate on the outer planets and their satellites. With the cratering rate, it will be possible to determine the age of the surface accurately (Greenstreet et al. 2015). Therefore, determining the abundance of the km-sized TNOs is essential for understanding the surface evolution of outer solar system bodies, especially of bodies in the Pluto system, whose surface conditions were recently revealed by the New Horizons spacecraft (Stern et al. 2015).

As of 2016, the size distribution of these small-sized TNOs is still unclear. So far, more than 1500 TNOs have been discovered by optical observations in the Kuiper belt and the scattered disk region (e.g. Jewitt & Luu 1993). However, these TNOs are larger than 10 km (e.g. Fraser & Kavelaars 2008), and no km-sized TNOs have been detected so far. Direct detection of km-sized TNOs is challenging because they are extremely faint, with typical optical magnitudes fainter than 28, and are thus undetectable even using telescopes with apertures ~ 10 m. Therefore, the size distribution of km-sized TNOs still remains an open question.

Instead of direct detection, monitoring of stellar occultation events is one possible way to discover km-sized TNOs. Since a TNO moves in the sky, it occasionally passes in front of stars and other point-like sources, changing the signal intensity from these objects by occultation. Several serendipitous studies of occultation events have been performed with ground- and space-based observatories and several optical studies have found possible occultation events. An analysis using high-cadence (40 Hz) photometry data of guide stars obtained with the guidance sensor onboard the Hubble Space Telescope has discovered two possible occultation events by sub-km-sized Kuiper belt objects (Schlichting et al. 2009, 2013). A very recent study by Liu et al. (2015) found 13 possible occultation events by sub-km-sized TNOs from time-sequence photometry data for asteroseismological studies obtained with the CoRoT satellite. While these studies have discovered possible occultation events by sub-km sized TNOs, there has been no detection of occultations by larger, km-sized TNOs, which are expected to be much less frequent events.

In order to detect stellar occultation events by km-sized TNOs for the first time, monitoring observations face several challenges. First, observations must monitor a large number of stars simultaneously to detect rare occultation events. Second, signals from stars must be sampled with a cadence faster than 10 Hz, because the durations of the occultations are expected to be smaller than

a second. Occultation observations thus require detector systems capable of achieving photometry with time resolution shorter than 0.1 seconds. Third, detections of stellar occultation events with ground-based instruments must be robust to atmospheric scintillation effects. Unlike space-based observations, ground-based monitoring observations suffer from atmospheric scintillation that can cause false positive detections.

This paper describes an approach to detect and explore TNO occultation events using multiple small observation systems. These multiple systems enable us to observe occultation events simultaneously and allow us to achieve detections that are robust with respect to atmospheric scintillation. The recent development of low-cost commercial CMOS detectors and powerful data storage allows us to create mobile observation systems providing wide-field and high-cadence observational data. As an example of the mobile observation systems, we discuss a project under current development for detecting serendipitous astronomical events, the Organized Autotelescopes for Serendipitous Event Survey (OASES). The OASES project plans to monitor known stars using multiple 30-cm-scale mobile telescopes with low-cost CMOS cameras placed on the Miyako Islands, Okinawa, Japan. Section 2 presents an overview of TNO occultations, reviewing the expected stellar light curve profiles for different sampling cadences. In Section 3, we describe the concept of the OASES project, and present the observation systems developed for the monitoring observations. The performance test observations and current monitoring observations together with the photometric performance of the OASES observation systems are presented in Section 4. Using the results of the monitoring observations, we have developed a new time calibration method for the time synchronization between the observation systems. The details of the calibration method are described in Section 5. Finally, we summarize the conclusions in Section 6.

2 General outline of the TNO occultation events

Starlight from an occulted star is diffracted by the edges of TNOs with their radii r less than 10 km because the sizes of the TNOs are comparable to the Fresnel scale, F , which is given by

$$F = \sqrt{\frac{R_h \lambda}{2}} \sim 1.3 \text{ km}, \quad (1)$$

where $R_h = 40$ au is the semi major axis of the TNO (R_h is approximated as the distance between the observer and the TNO in this equation), and $\lambda = 500$ nm is the wavelength of the observations.

As described in detail by Nihei et al. (2007), the observed light curve for an occultation event is determined by the size, shape, and distance of the TNO, the angular size of the star, the impact parameter between the star and the TNO, the wavelength range of the observations, and the relative

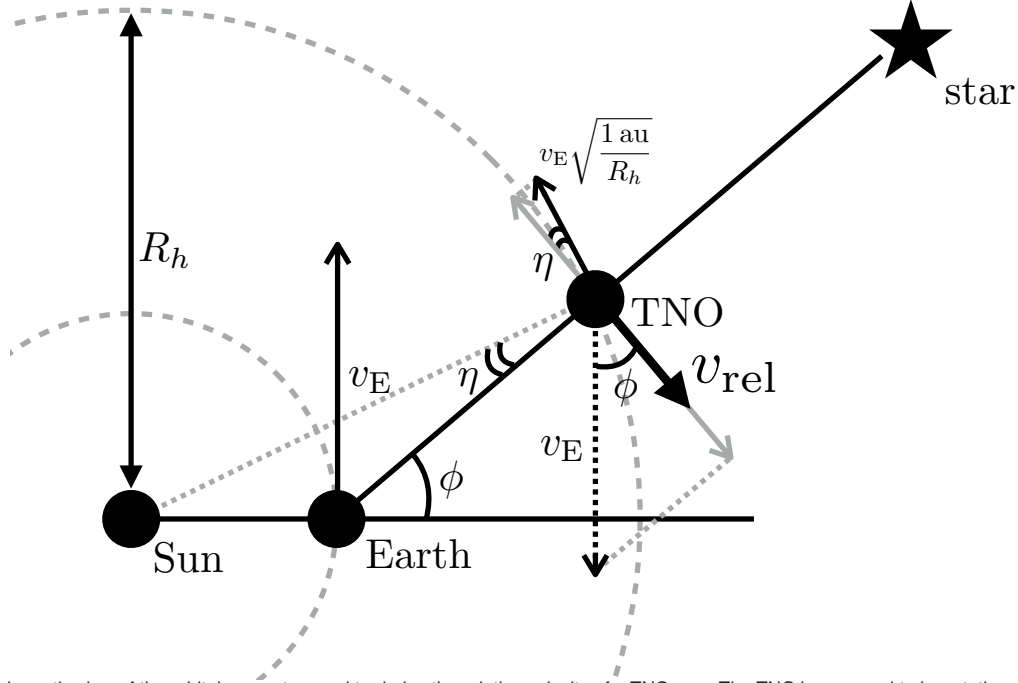


Fig. 1. Schematic view of the orbital geometry used to derive the relative velocity of a TNO v_{rel} . The TNO is assumed to be rotating on a circular ecliptic orbit with a radius of R_h .

velocity between the observer and the TNO. According to the simulations by Nihei et al. (2007), the duration of the event is determined by the length of the occulter passing in front of the star and the relative velocity. The occulter length L passing in front of a star is described by

$$L = \sqrt{W^2 - (2b)^2}, \quad (2)$$

where b is the impact parameter and W is the diameter of the occulter, which is determined by the radius of the TNO and the diffraction effects. Assuming a spherical TNO with a radius r , W is approximated by Nihei et al. (2007) as

$$W \sim \left[(2\sqrt{3}F)^{3/2} + (2r)^{3/2} \right]^{2/3}, \quad (3)$$

which corresponds to the diameter of the first Airy ring. We should note that W does not become smaller than $2\sqrt{3}F$, corresponding to ~ 5 km for a TNO located in the Kuiper belt ($R_h = 40$ au). On the other hand, assuming a TNO on a circular ecliptic orbit with a radius of R_h (see figure 1), the velocity of the TNO relative to the Earth, v_{rel} , is given by

$$v_{\text{rel}} = v_E \cos \phi - v_E \left(\frac{1 \text{ au}}{R_h} \right)^{1/2} \cos \eta = v_E \left[\cos \phi - \left(\frac{1 \text{ au}}{R_h} \right)^{1/2} \left(1 - \frac{1 \text{ au}^2}{R_h^2} \sin^2 \phi \right)^{1/2} \right], \quad (4)$$

where v_E is the orbital velocity of the Earth (29.8 km s^{-1}) and ϕ and η are the TNO–Earth–opposition

and the Sun–TNO–Earth angles in the ecliptic plane, respectively (see figure 1). Since the orbital velocity of the TNO is less than 5 km s^{-1} and is much smaller than v_E , v_{rel} mostly depends on ϕ . The duration of the occultation event, τ , is given by

$$\begin{aligned} \tau &= \frac{W}{v_{\text{rel}}} & (5) \\ &= \left(\frac{1}{v_E}\right) \left[\left[(2\sqrt{3}F)^{3/2} + (2r)^{3/2} \right]^{4/3} + (2b)^2 \right]^{1/2} \left[\cos\phi - \left(\frac{1\text{au}}{R_h}\right)^{1/2} \left(1 - \frac{1\text{au}^2}{R_h^2} \sin^2\phi\right)^{1/2} \right]^{-1} & (6) \end{aligned}$$

If a TNO located at opposition ($\phi = 0$) occults a star with $b = 0$, the duration of the occultation event τ is

$$\tau \simeq 0.2 \left[1 + \left(\frac{r \text{ [km]}}{2.5} \right)^{3/2} \right]^{2/3} \text{ [sec]}. \quad (7)$$

τ is thus determined by the size of the TNO and is expected to be about 0.2–0.9 seconds for a km-sized TNO (with $r = 1 - 10 \text{ km}$). Therefore, observations with time resolution better than 10 Hz are required for robust detection of these occultation events.

Figure 2a shows the expected light curve of a $V = 13.0$ mag F6V star occulted by a $r = 1.5$ km sized TNO located at 40 au and traversed at an impact parameter $b = 0$. The light curve shows clear diffraction features; the local peak is seen at the occultation center, and the intensity is enhanced at the edges of the shadow corresponding to the first Airy ring. Figure 2b presents the same light curve as figure 2a but sampled at 5 Hz; the same sampling cadence as that of the previous ground-based coordinated occultation observations, Taiwanese American Occultation Survey (TAOS, Lehner et al. (2009)). Since the time interval of the occultation is only $\sim 0.2 \text{ sec}$, the outlier of the light curve due to the occultation event is only detected in one or two bins. Therefore we cannot obtain the information on the duration of the occultations, which provides a constraint on the size information of the occulters. In order to gain a clear constraint of the size of the TNOs, we have to obtain the stellar light curves with time resolution comparable to, or higher than, $\sim 10 \text{ Hz}$ (figure 2c). In fact, ongoing and proposed TNO occultation observation projects such as CHIMERA (Harding et al. 2016), TAOS II (Lehner et al. 2014), and the present OASES projects plan to monitor stars with sampling cadences of 15 – 30 Hz.

As already noted in section 1, stellar occultation by km-sized TNOs is expected to be very rare. According to the results of the previous TAOS observations (Bianco et al. 2010; Zhang et al. 2013), the event rate of the occultation is expected to be less than 10^{-2} yr^{-1} per star, much smaller than that of the sub-km sized TNO occultations (Schlichting et al. 2013). Therefore serendipitous surveys should monitor more than hundreds of stars simultaneously, and thus require a wide field. Furthermore, since stellar occultations by unknown TNOs are short-timescale and non-repeatable phenomena, the atmospheric scintillation and other noise can cause false detection. In order to avoid

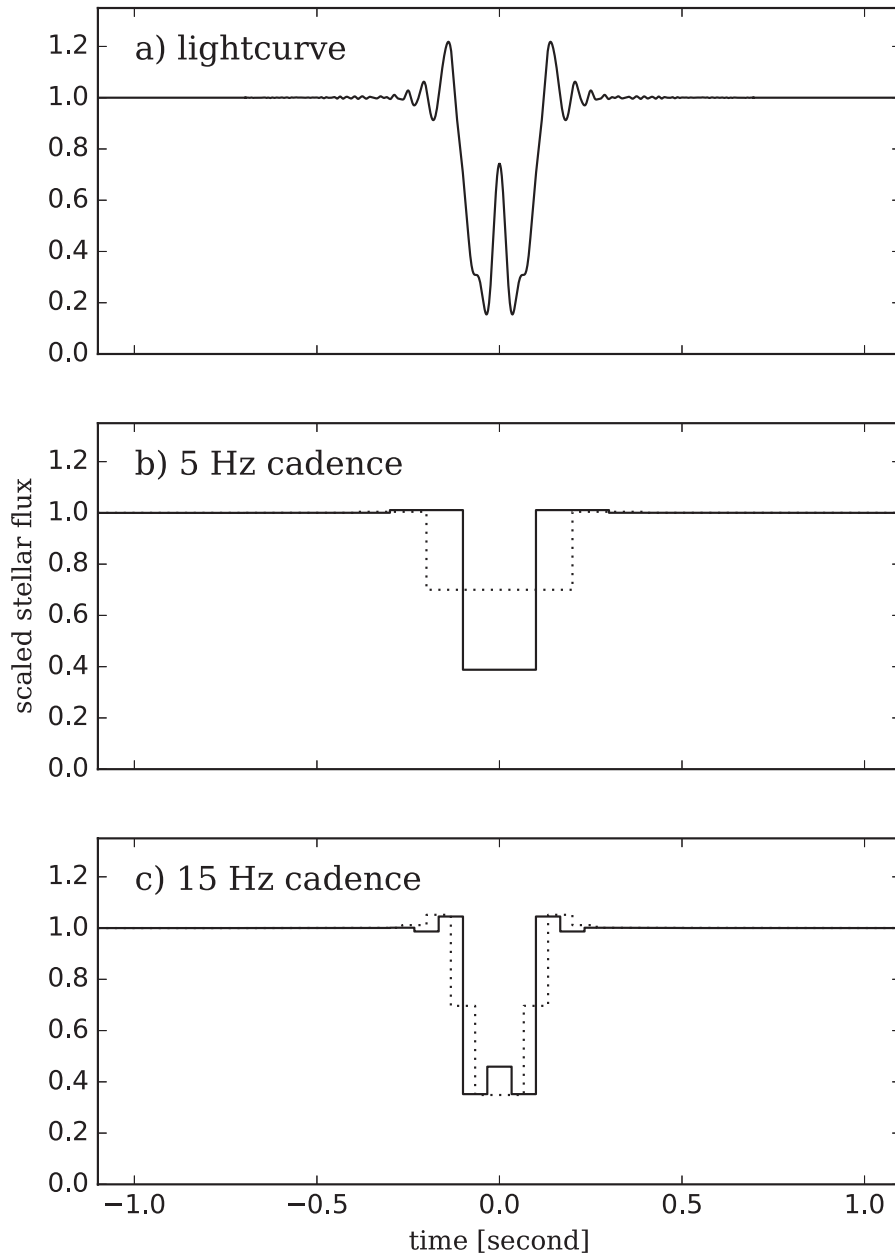


Fig. 2. (a): Simulated light curve of an occultation event for a $r = 1.5$ km sized TNO located at $R_h = 40$ au, and traversed at impact parameter $b = 0$. The occultation is assumed to occur at $\phi = 30^\circ$, and is observed at a wavelength of 500 nm. The background object is assumed to be a $V = 13$ mag F6V star. The finite size of the star is taken into consideration. (b) and (c): The same light curve as (a), but sampled at a cadence of (b) 5 Hz and (c) 15 Hz. Solid and dotted lines in panels (b) and (c) show light curves of the occultation sampled with no time offset and with a time offset of $1/10$ and $1/30$ seconds, respectively.

false detection due to noise, simultaneous detection by multiple instruments is essential for stellar occultation observations. Increasing the number of observation instruments will offer more robust detection of stellar occultation events because the probability of the false-positive detection significantly decreases with the number of independent observation data obtained simultaneously (Lehner et al. 2010). One of the challenges for the installations of the multiple instruments is to realize their low-cost production; the total cost of the observation project increases almost linearly with the number of instruments. Therefore the development of multiple low-cost instruments has a key role in the achievement of coordinated monitoring observations.

3 Outline of the OASES observation system

The OASES project uses multiple observation systems, each containing a commercial monochromatic CMOS camera and an optical tube for astronomical photographs. This section describes the observation system and the current observation site of the OASES project. Hardware specifications of the current OASES observation system are summarized in table 1. The principal advantage of the system is its cost effectiveness. Since commercial off-the-shelf optics and CMOS cameras are adopted, an installation of a single OASES observation system costs about 16000 US \$. This advantage makes it possible to install a large number of multiple observation systems with limited financial resources. As of September 2016, the OASES project exploits two observation systems (OASES-01 and OASES-02) and plans to increase the total number of systems in the near future.

3.1 Camera component

The OASES observation system employs a ZWO Co., Ltd. ASI1600MM-Cool monochromatic CMOS camera. This camera has a MN34230 front-illuminated CMOS sensor manufactured by the Panasonic Corporation. The CMOS sensor consists of 4656×3520 square pixels with a pixel pitch of $3.8 \mu\text{m}$, offering a $17.7 \text{ mm} \times 13.4 \text{ mm}$ effective area. According to the manufacturer of the CMOS sensor (<https://industrial.panasonic.com/content/data/SC/PDF/news2013/jp/IS00006AJ.pdf>), each pixel of the CMOS sensor includes a microlens to increase the effective photon collecting area. Since the spectral response of the CMOS camera is not supplied by the manufacturer in detail, it was measured using a quantum efficiency (QE) measurement bench (Kamata et al. 2004). The relative spectral response of the camera detector normalized at the peak (at 510 nm) is shown in figure 3. According to the manufacturer (<https://astronomy-imaging-camera.com/products/usb-3-0/asi1600mm-cool/>), the absolute peak QE is $\sim 60\%$. The camera provides an efficiency of over 50% of the peak value (corresponding to

Table 1. Specifications of the OASES prototype and observation systems

Observation system	prototype system	observation system
Number of systems	1	2
Optics	Celestron, LLC. Rowe-Ackermann Schmidt astrograph	
Aperture [mm]	279	
Focal Ratio	f/2.22	f/1.58
Camera	Point Grey Research, Inc. <i>grashopper 3 GS3-U3-23S6M-C</i>	ZWO Co., Ltd. ASI1600MM-Cool
Number of effective pixel	1920 × 1200	4656 × 3520
pixel size [μm]	5.86	3.8
Angular pixel scale [arcsec pixel ⁻¹]	1.96	1.79 (3.59 :2 × 2 binned mode)
Field of view [degree ²]	0.68	4.05
Readout noise [e^-]	6.8	2.9
Quantum efficiency [% at 525 nm]	76	~ 60
Mount	Takahashi Seisakusho Ltd. EM-200 <i>Temma-2 Jr.</i> German equatorial mount	

~ 30% absolute QE) over the wavelength range of 400 – 750 nm. The lower QE relative to those of the scientific-grade CCD sensors (typically > 50% absolute QE over the wavelength range of 400 – 800 nm) is most likely due to a smaller photon collecting area limited by readout electronics on the front-illuminated CMOS sensor. The ASI1600MM-Cool CMOS camera has a two-stage Peltier cooler to maintain the CMOS sensor with an operating temperature at 5 – 10 °C.

3.2 Optical component

The optical component of the OASES observation system is a Celestron, LLC. Rowe-Ackermann Schmidt Astrograph (RASA). The RASA is a prime-focus astrograph with an effective aperture diameter of 279 mm, and focal ratio $f/2.22$. The primary advantage of the RASA is that it provides a wide optical field of view (FOV) with a very fast focal ratio. A Celestron, LLC. publication (Berry et al. 2016) lists the designed image circle diameter of the astrograph as $\phi = 43.3$ mm, which corresponds to a FOV of 4.00° across (12.6 degree² area).

Although the RASA provides a wide field with the fast focal ratio, it is too large for the CMOS sensor of the OASES camera component. Taking the focal length of the RASA (620mm) and the effective area of the ASI1600MM-Cool CMOS camera (17.7 × 13.4 mm) into account, the FOV covered by the CMOS sensor is 1.64° × 1.24° (2.02 degree² area), which is much smaller than

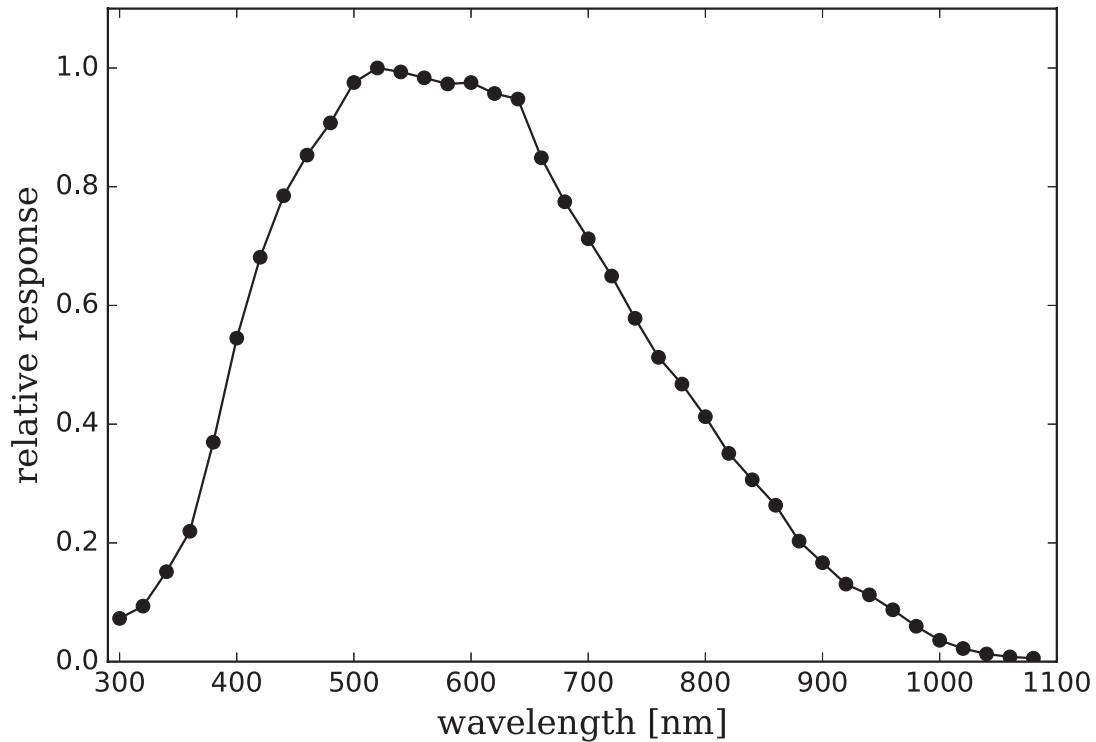


Fig. 3. The measured relative spectral response of the ZWO Co., Ltd. ASI1600MM-Cool CMOS camera. The response is normalized at the peak.

the optically flat FOV provided by the RASA optics (12.6 degree² area). In order to increase the instrumental FOV and to improve the efficiency of monitoring observations, we insert a focal reducer between the RASA and the CMOS camera. The Metabones Speed Booster SPEF-M43-BT4 is used as a focal reducer. Since the variable ratio of the focal reducer is 0.71, the effective focal length is 440 mm (focal ratio = $f/1.58$). The Speed Booster offers a corrected focal plane covering the effective area of the CMOS sensor, and increases the FOV of the observation system to $2.32^\circ \times 1.75^\circ$ (4.05 degree² area). However, we found that the illumination of the system drops by approximately 60% from the image center to the edge. We thus generally use the central $\sim 1^\circ$ -radius field, over which the illumination drops by only $\sim 20\%$.

In the present observations, no filter wheel is used with the observation system. However, we plan to install an additional filter holder in front of the focal reducer in future observations.

3.3 Functional overview and control software

A functional overview of the OASES observation system is presented in figure 4. The individual observation system is mounted on a Takahashi Seisakusho Ltd. EM-200 *Temma-2 Jr.* German equatorial



Fig. 4. A functional overview of the OASES observation system. The ZWO Co., Ltd. ASI1600MM-Cool CMOS camera is mechanically connected to the Celestron, LLC. RASA via the Metabones Speed Booster focal reducer. The CMOS camera and the mount are connected to the same control PC via USB and Thunderbolt-RS232C connections using Thunderbolt to USB and USB to RS232C adapters, respectively. The 100 V AC power is supplied to all the electrical devices in the system.

mount. The CMOS camera and the equatorial mount are controlled by the same control PC. In the present observations, tracking is performed in open loop mode (without feedback from any guiding facility). According to the results of the observations, the typical root-mean-square tracking accuracy of the mount is $\sim 14''$ for 30 minutes. The CMOS camera is set up with *Firecapture* version 2.4, an image capture program for USB-connected cameras (see <http://firecapture.wonderplanets.de>). The user can control the camera parameters, and obtain imaging data with user-defined exposure times and number-of-frames by running command scripts on the software. The images obtained are recorded on a SSD storage, which is connected to the control PC via a Thunderbolt connection. The equatorial mount is controlled via a proprietary program, *StellaNavigator* version 10 (see <https://www.astroarts.co.jp/products/software.shtml>). The user points the observation system to the desired position using the program.

A GPS receiver connected via USB is used as a source for time synchronization of the control PC. The internal clock of the control PC is synchronized with the GPS time information received from the GPS receiver using *Satk* version 3.4 time adjustment software (see <http://sendaiuchukan.jp/>

data/occult/gpsradio/satk.html). The *Firecapture* software writes timestamps for individual frames in the header information of the imaging data (SER file). The equatorial mount, the CMOS camera, the control PC and the SSD storage are powered by the same 100 V AC power supply.

3.4 Observation site

The two OASES observation systems are currently installed at an observation site in Miyako Island (figure 5a and 5b), Miyakojima-shi, Okinawa prefecture, Japan (Miyako open-air school (*Miyako Seishonen no Ie*), latitude: $24^{\circ} 48' 17''\text{N}$, longitude: $125^{\circ} 18' 55''\text{E}$, altitude: 33 m, marked as an open circle in figure 5b). Since Miyako Island is at $24 - 25^{\circ} \text{N}$ ($\sim 10^{\circ}$ farther south than the major islands of Japan), it is one of the most appropriate sites in Japan for the observation of objects near the ecliptic. In addition, according to the results of the present monitoring observations, the ratio of fine weather is $\sim 40\%$ for the period from late June to early September during which the selected observation field (see subsection 4.2) is visible. This fine weather ratio is higher than at other major observation sites in Japan. Furthermore, in this period, the island is almost free from strong jet streams, which often cause turbulence and may increase atmospheric scintillation effects.

4 OASES observations

4.1 Performance test observations

OASES performance test observations were carried out in 2015 with a single prototype system. Specifications of the prototype are presented in table 1. The prototype was designed with the same optical components as the current system. However, it is coupled with a small-format CMOS sensor (SONY Corporation IMX174) without a focal reducer and provides images with a narrower field-of-view ($1^{\circ}.05 \times 0^{\circ}.65$). The prototype system was placed at "Toriba Kaihin Koen" park on Miyako Island (latitude: $24^{\circ} 48' 10''\text{N}$, longitude: $125^{\circ} 15' 23''\text{E}$, altitude: 1 m, marked as an open square in figure 5b), and observed dense stellar fields as proof-of-concept observations.

4.2 Monitoring observations

The first scientific monitoring observations for stellar occultation began on 25 June 2016 with the two OASES observation systems. The two systems were placed in different positions on the rooftop of the Miyako open-air school (*Miyako Seishonen no Ie*; marked as an open circle in figure 5b, see also figure 6). The two systems were 39 m apart (see Figure 5c). We carried out monitoring for 40 hours in total, over the period from 25 June to 10 September JST.

For the monitoring observations, we selected a target sky region with the following criteria.

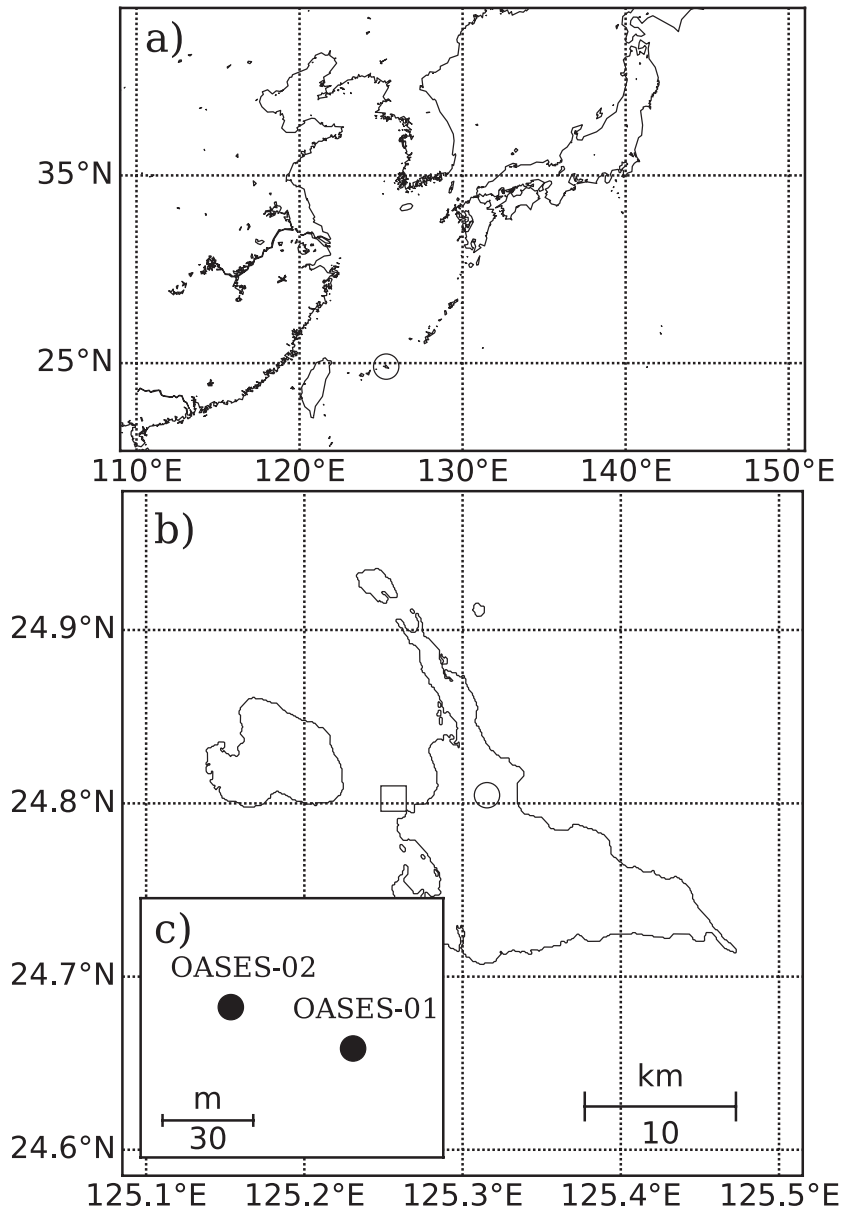


Fig. 5. (a) Map of East Asia with location of Miyako Island (open circle). (b) Map of Miyako Island overlaid with the OASES monitoring site (Miyako open-air school: open circle), where the monitoring observations were performed in 2016, and the site of the performance test observations in 2015 (*Toriba Kaihin Koen* park: open square). Since the *Toriba Kaihin Koen* park was built over reclaimed shoreline, it appears to lie over the sea. In (a) and (b), the coastline data provided with the Basemap Matplotlib Toolkit version 1.0.8 (<http://matplotlib.org/basemap/index.html>) are used. (c) The layout of the two OASES observation systems (OASES-01 and OASES-02) at Miyako open-air school.

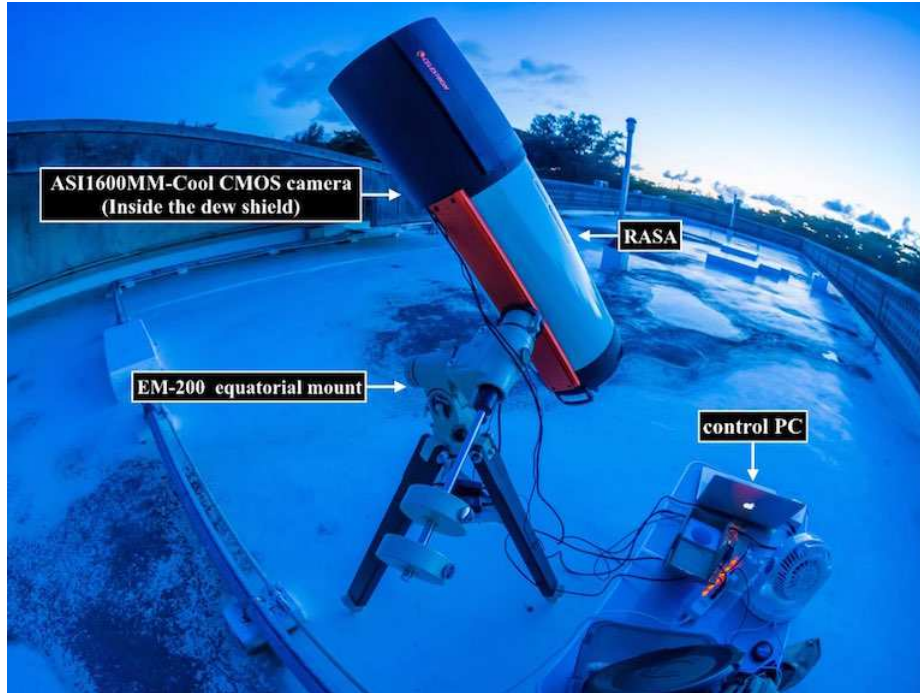


Fig. 6. The OASES observation system (OASES-02) installed at Miyako open-air school, Miyakojima-shi, Okinawa. The system, which consists of a Celestron, LLC. RASA optical tube attached to a ASI1600MM-Cool CMOS camera (hidden by a dew shield in this image), is mounted on a Takahashi Seisakusho Ltd. EM-200 German equatorial mount .

Since the chance of occultation increases with the number of stars observed simultaneously, we selected fields that contain a large number of stars with V-band magnitudes (m_V) brighter than 14.0 mag. The selected fields are thus close to the Galactic plane. On the other hand, most of the Kuiper belt objects are expected to be located near the ecliptic (Elliot et al. 2005). Thus we searched for regions that lie within 2° of the ecliptic. These criteria gave a monitoring observation field with equatorial and ecliptic coordinates of $(\text{RA}, \text{Dec}) = (18 : 30 : 00, -22 : 30 : 00)$ and $(\lambda, \beta) \sim (276^\circ.9, +0^\circ.8)$, respectively.

Images of the selected field are obtained simultaneously with the two observation systems for a 2×2 binned sequential shooting mode of 15.4 frames every second. The exposure time is 65.0 milliseconds for each frame. Eight 16-bit uncompressed SER video files (see <http://www.grischa-hahn.homepage.t-online.de/astro/ser/>) each consisting of 3300 images are produced as a "SER data group" consisting of 26400 images by one capture procedure.

4.3 Data reduction

We developed the OASES prototype data reduction pipeline, a Python-based image processing program, for data reduction of the monitoring observations. A functional overview of the pipeline is

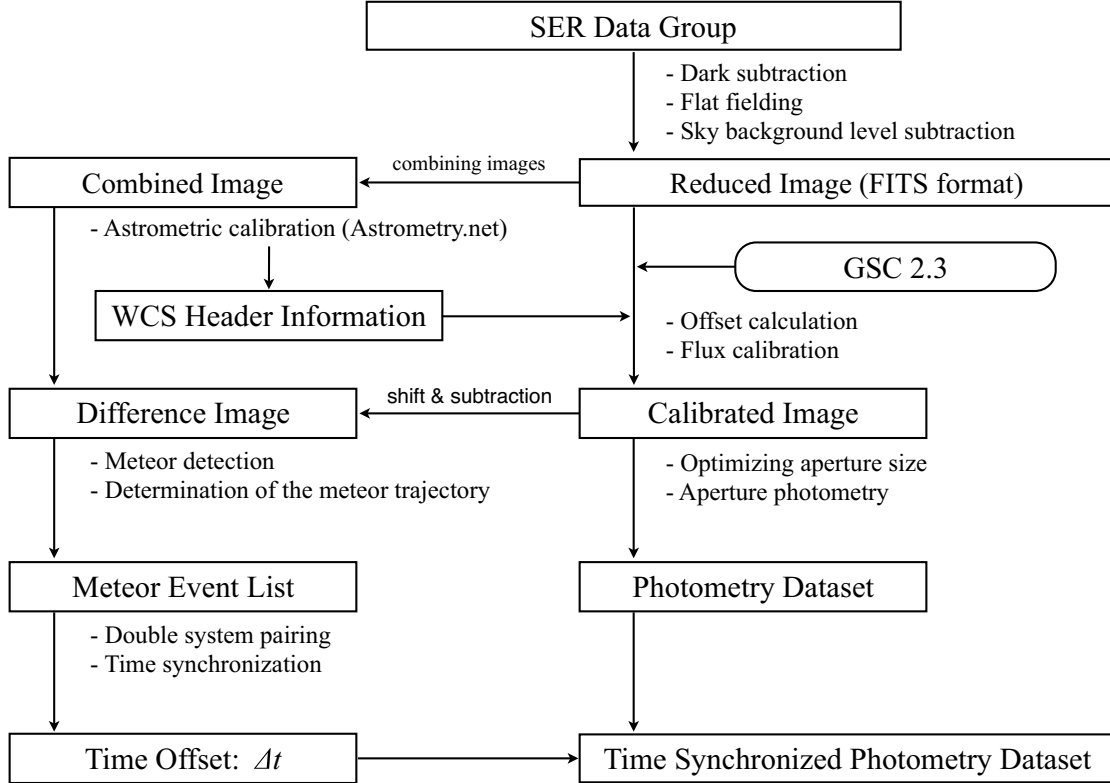


Fig. 7. Functional overview of the OASES data reduction pipeline.

shown in figure 7. The reduction methods adopted for the pipeline are based on the TAOS data reduction procedures (Zhang et al. 2009) and are adapted for the OASES observations. The first stage of the pipeline includes dark subtraction using dark frames, flat-fielding using twilight flat frames, and subtraction of a constant sky background level, to produce FITS-formatted reduced images. An example of the reduced image obtained after these procedures is shown in figure 8a. The full-width half maximum of stars in the images is typically $9 - 11''$, which corresponds to \sim six physical pixels and \sim three image pixels.

A hundred reduced images in every SER data group (the 9901st to 10000th out of the total of 26400 images) are selected as a sample of the data and are averaged to create a combined image. An astrometric calibration for the combined image is performed using the *Astrometry.net* version 0.67 calibration software (Lang et al. 2010). Using the World Coordinate System (WCS) parameters obtained after the astrometric calibration, the pixel coordinates of the stars in the combined image are derived with the Guide Star Catalogue (GSC) version 2.3 (Lasker et al. 2008). In each frame, pixel coordinates of the stars usually change with time due to tracking imperfections of the equatorial mount. Therefore we derive barycenters of 30 unsaturated bright stars in each frame to calculate an offset of the pixel coordinates on each epoch.

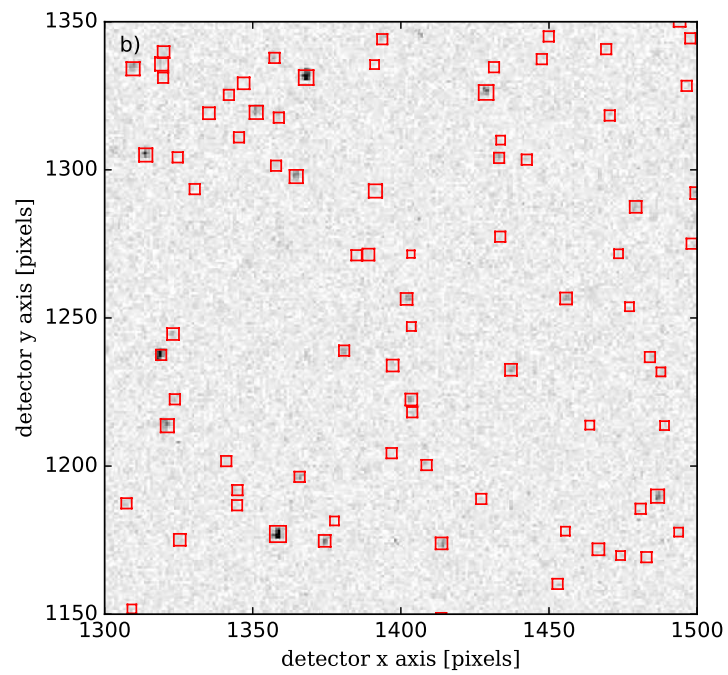
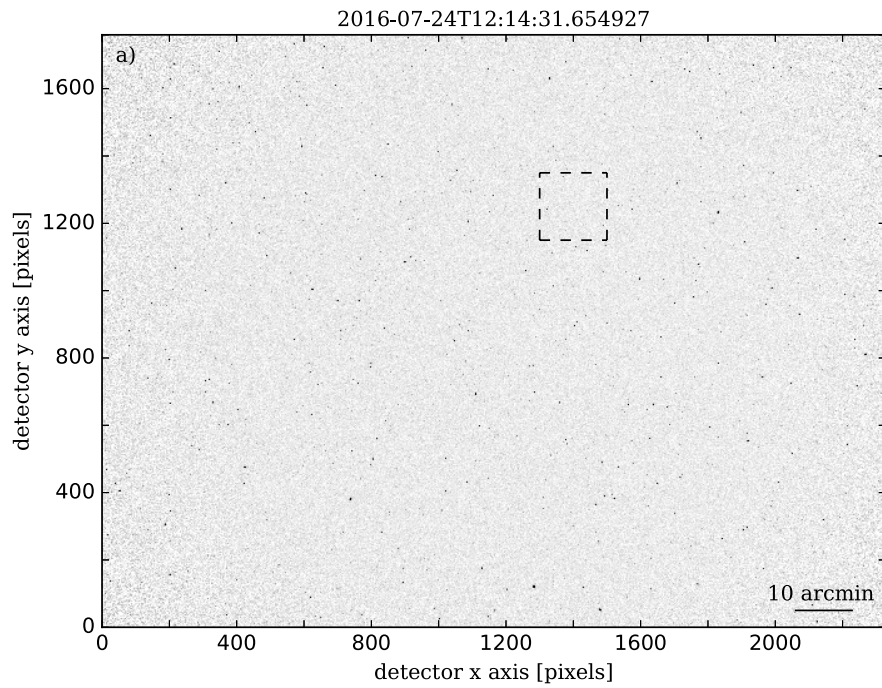


Fig. 8. Example of an image obtained in the performance test observations. (a) The one-frame reduced image obtained after the dark-subtraction, the flat-fielding, and background subtraction procedures. (b) Enlargement of the image (dashed square in panel (a)), overlaid with the optimal aperture masks for individual stars (red open squares).

With the pixel coordinates of the GSC stars for each frame, we perform aperture photometry for the individual stars with m_V brighter than 14.0 mag. Square apertures with sizes A are chosen as photometry apertures for computational efficiency, and a square annulus with a width of g times of the aperture size is selected as a local background region for each star. The median value of the pixels in the local background region is subtracted from the aperture pixels as a background level before integrating to produce a signal value. The sizes of the square aperture A and the background annulus parameter g for each star are chosen to optimize the signal-to-noise performance of the resulting light curves. The aperture-size optimization procedure is based on the data reduction method for TAOS (Zhang et al. 2009). We perform aperture photometry for each star in the 200 (9901st to 10100th) reduced images in each SER data group with different aperture and background annulus sizes. Then we obtain a light curve of 200 data points for each photometry parameter set (A, g) . After that, we calculate the average intensity \bar{I} and the standard deviation of the intensity $\sigma(I)$ for each light curve to derive the signal-to-noise ratio for the light curve (hereafter *light curve S/N*), $\bar{I}/\sigma(I)$. We analyze the light curve S/N as a function of A and g for each star. The minimum aperture size A_{\min} of this calculation is chosen to be 2 pixels. The maximum aperture size A_{\max} is determined by the following criteria in order to minimize contamination from neighboring stars. When performing photometry of a star of m_V at a pixel coordinate (X, Y) , we consider neighboring stars with V-band magnitudes brighter than $(m_V + 1.5)$ mag. For any neighboring star i located at (x_i, y_i) , we select the maximum square size A_{\max} smaller than the maximum value of two absolute values, $|2(X - x_i)|$ and $|2(Y - y_i)|$. In the present data reduction pipeline, A_{\max} is chosen in steps of 0.5 pixels from 3.5 to 8 pixels. If any contaminating star is located within a 3.5-pixel square aperture, we did not perform photometry of the target star (corresponding to $\sim 6\%$ of the total field stars in the selected field).

For each star, we perform square aperture photometry with aperture sizes A from 2.0 to A_{\max} pixels in steps of 0.5 pixels and background annulus parameter g from 0.5 to 1.0 in steps of 0.25. In the present observations, about 80% of the stars have one or more local maxima of the light curve S/N. We adopt the aperture size where the light curve S/N reaches the local maximum, or the aperture size that gives the minimum of the local S/N maxima, as the optimized aperture size to minimize contamination from neighboring stars and noise. There are cases when the light curve S/Ns increase or decrease monotonically. In these cases, we adopt the maximum or minimum sizes as the optimized aperture sizes, respectively. Figure 8b shows an example of the selected apertures for individual stars overlaid on the reduced image.

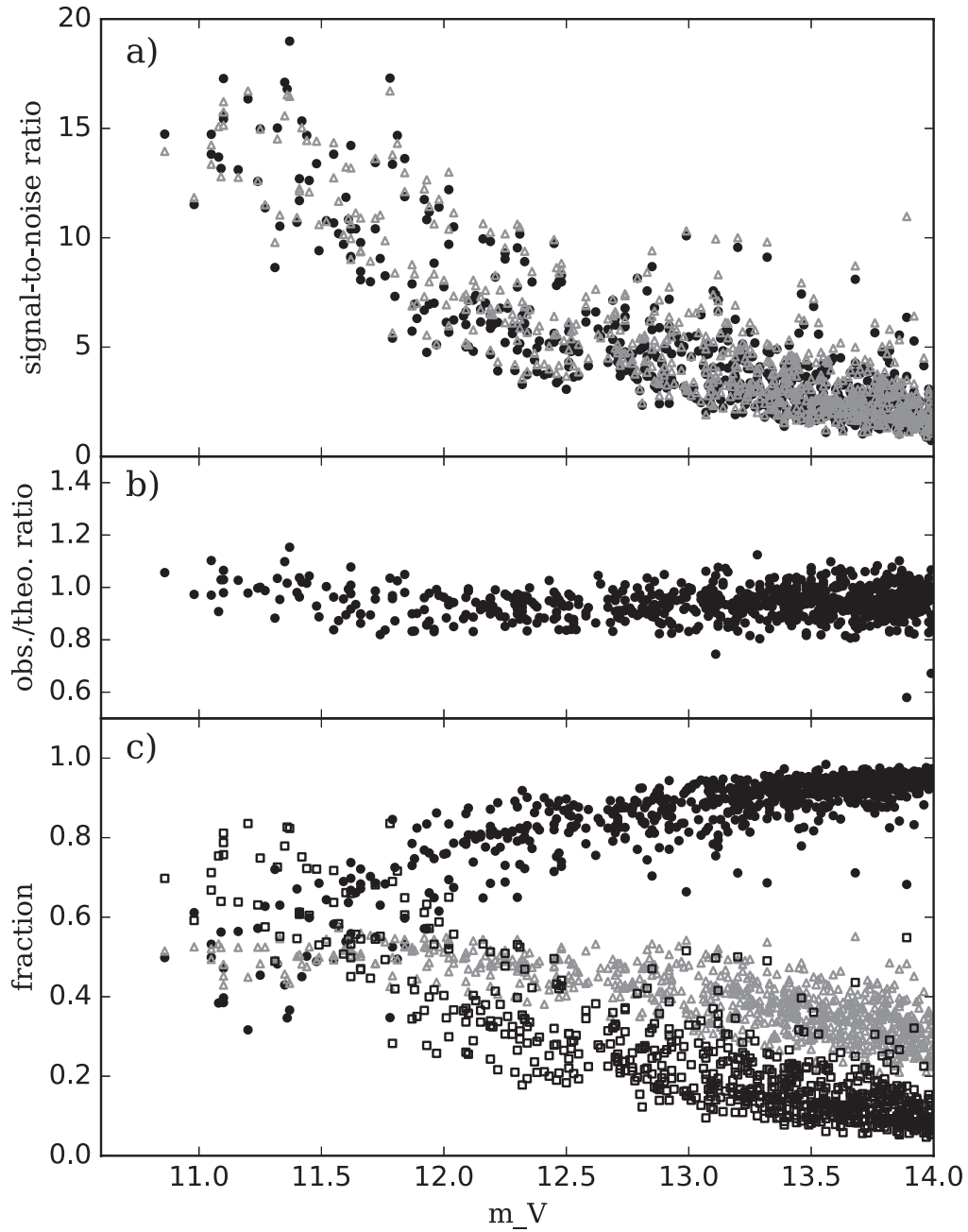


Fig. 9. (a) Example of light curve S/N values obtained in the OASES monitoring observations on a dark night (filled black circles) and theoretical S/Ns (open grey triangles) as a function of m_V . Only a sample of 8% of all stars is shown for clarity. In this plot, η is assumed to be 0.05. (b) Observed light curve S/Ns scaled by the theoretical light curve S/Ns. (c) The variance of major noise sources; the readout noise (σ_{read} ; filled black circles), the target shot noise (σ_{source} ; open grey triangles), and the scintillation noise (σ_{sci} ; open black squares), scaled by the total theoretical noise.

4.4 Photometry results

Figure 9a shows an example of the light curve S/Ns obtained from the OASES monitoring observations (plotted as black filled circles). The average S/N value reaches 3, 5, and 10 at $m_V \sim 13.5$, 12.8, and 11.8, respectively. In order to characterize the noise performance of the OASES observation system, we compare the observed light curve S/Ns with the theoretical S/N values for the individual stars. In general, the light curve S/N for a star obtained with high-cadence observations using an optical photoelectric detector array would be approximated by the following equation:

$$\text{theoretical } S/N = \frac{S_{\text{star}}}{\sqrt{\sigma_{\text{read}}^2 + \sigma_{\text{dark}}^2 + \sigma_{\text{sky}}^2 + \sigma_{\text{source}}^2 + \sigma_{\text{sci}}^2}} \quad (8)$$

where S_{star} is the signal values of a star obtained with the square aperture size A in e^- . σ_{read} , σ_{dark} , σ_{sky} , σ_{source} , and σ_{sci} represent the detector readout noise, the dark noise, the sky background noise, the target shot noise, and the scintillation noise, respectively, which are expressed as follows:

$$\sigma_{\text{read}}^2 = \sigma_{\text{readpix}}^2 A^2, \quad (9)$$

$$\sigma_{\text{dark}}^2 = i_{\text{dark}} A^2, \quad (10)$$

$$\sigma_{\text{sky}}^2 = s_{\text{sky}} A^2, \quad (11)$$

$$\sigma_{\text{source}}^2 = S_{\text{star}}, \quad (12)$$

$$\sigma_{\text{sci}}^2 = \eta^2 S_{\text{star}}^2, \quad (13)$$

where σ_{readpix} is the standard deviation of the detector readout noise in $e^- \text{ pix}^{-1}$, i_{dark} is the dark current for the observed exposure time (65 milliseconds) in $e^- \text{ pix}^{-1}$, s_{sky} is the surface brightness of the sky background in $e^- \text{ pix}^{-1}$, and η is the fractional scintillation variance relative to S_{star} . A^2 corresponds to the effective number of pixels for the square aperture photometry size A .

According to the laboratory tests, σ_{readpix} is estimated to be $5.8 e^- \text{ pix}^{-1}$ in the 2×2 binned mode. On the other hand, i_{dark} is estimated to be smaller than $0.1 e^- \text{ pix}^{-1}$ at the operating sensor temperature ($5 - 10^\circ \text{C}$). The contribution of σ_{dark}^2 relative to σ_{read}^2 can thus be considered negligible. s_{sky} is determined from the $3\text{-}\sigma$ clipped average pixel values of images obtained in the observations. The measured s_{sky} is $5 - 10 e^- \text{ pix}^{-1}$, and thus σ_{sky}^2 is insignificant relative to the σ_{read}^2 .

The theoretical light curve S/Ns for the individual observed stars are plotted as open triangles in figure 9a and are compared with the observed S/Ns in figure 9b. In figure 9, η is approximated as 0.05. According to the comparison between the theoretical S/Ns and the observed values, the ratio of observation to theoretical S/N approaches unity when the fractional scintillation variance η is taken as $0.05 - 0.1$. This fractional variance is consistent with that obtained in the performance test observations of bright stars ($\sim 0.05 - 0.08$, see subsection 4.1). With this η value, the observed light

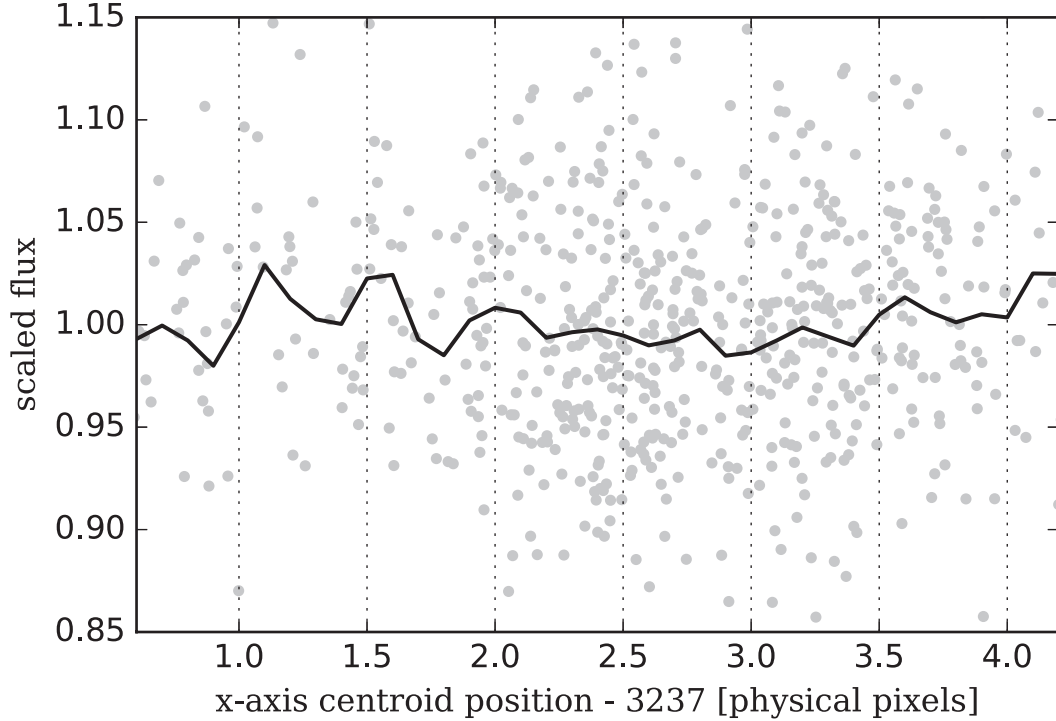


Fig. 10. Example of a scatter plot showing the measured fluxes of a bright star (TYC 6857-238-1, $m_V = 10.7$) scaled by their average value against the centroid positions in the x-axis direction of the CMOS sensor. In this example, the star moves in the hour angle direction (parallel to the x-axis direction of the CMOS sensor) in a two-minute observation due to tracking imperfections of the mount. A solid line represents moving average of the fluxes with a window of 0.1 pixels. The standard deviation of the fluxes and of their moving average values are 0.058 and 0.014, respectively. For the data points used in the plot, the relative differences of the positions in the y-axis direction are smaller than 0.2 pixels.

curve S/Ns are well approximated by the theoretical performance. Figure 9c shows the variance of each major noise source (σ_{read} , σ_{source} , and σ_{sci}) scaled by the total theoretical noise. At the flux range of $m_V \sim 12 - 14$, the detector readout noise is the dominant noise source. On the other hand, at the brighter flux range ($m_V < 11.5$), the target shot noise and the scintillation noise become comparable with the readout noise.

The measured stellar flux may be affected by non-uniformity of sensitivity within the pixel, because the OASES observation system uses a commercial front-illuminated CMOS sensor, in which readout electronics decreases the photon collecting area within the pixel. It can cause a systematic error on the flux with imperfect tracking and degrade the detectability of stellar occultations. In order to examine how the non-uniformity within the pixel affects the stellar flux measurements, we carried out a comparison between the measured flux values of a bright star and their centroid positions obtained in the monitoring observations with imperfect tracking. An example of a scatter plot of the measured fluxes against the centroid positions of a bright is shown in Figure 10. This plot shows

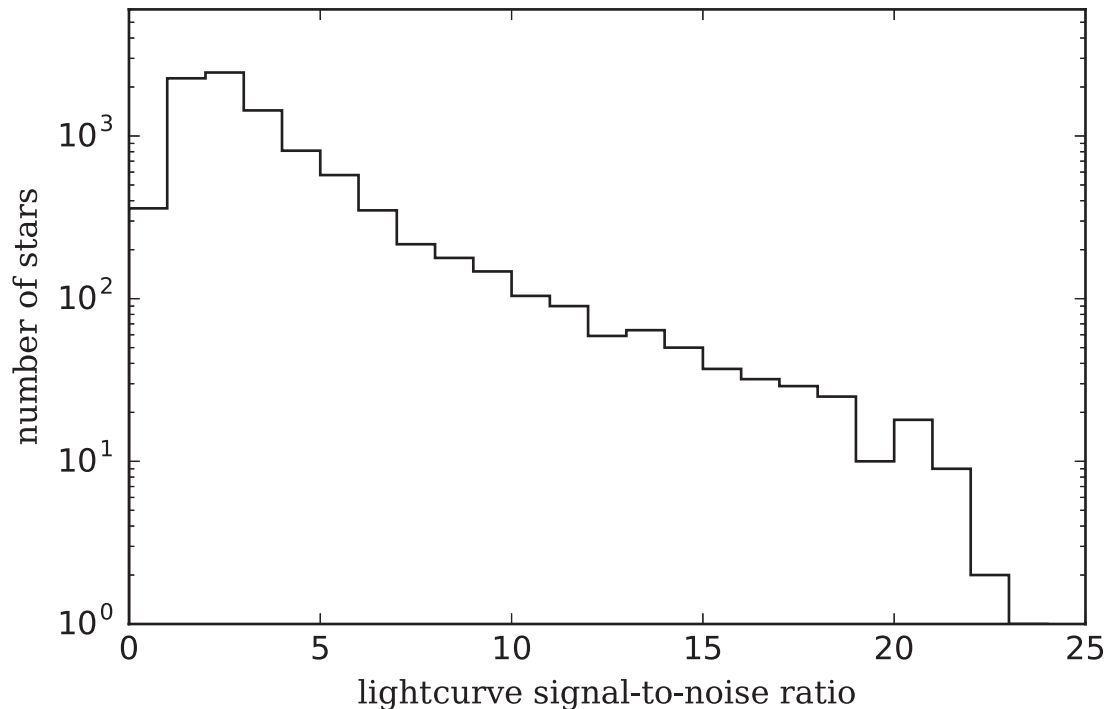


Fig. 11. Histogram of the number of stars observed simultaneously with the OASES observation system as a function of the light curve S/N.

no clear trend of the flux with an amplitude greater than $\sim 2\%$ of the average flux values. The systematic uncertainty is thus significantly small compared to the depth of the stellar occultations by km-sized TNOs (typically larger than 20%) and is expected to be negligible for the current occultation observations.

Figure 11 shows the histograms of the number of stars simultaneously observed with the OASES observation system as a function of the light curve S/N. For the selected observation field, the observation system is capable of monitoring ~ 500 , 2000, and 4200 stars with light curve S/Ns greater than 10, 5, 3, respectively. According to Nihei et al. (2007), the detectability of the occultation depends highly on the TNO size, the sampling rate of the observation, and the light curve S/N. Assuming a stellar occultation by a Kuiper-belt ($R_h = 40$ au) TNO at opposition observed with the two OASES observation systems at a sampling rate of 15.4 Hz, an occultation event by a TNO with a radius r of greater than ~ 1 , 1.5, and 3 km can be detected from light curves with the light curve S/N of 10 and 5, and 3, respectively, with the false positive rate lower than 10^{-11} . Therefore stellar occultations by km-sized TNOs are detectable with the light curves. In the previous coordinated observations (TAOS), the number of stars that could be monitored simultaneously was up to ~ 1000 (Lehner et al. 2010) with a sampling rate of 5 Hz. Therefore the OASES observation system is capable of monitoring a larger number of stars simultaneously with the greater sampling cadence and will

provide the statistically useful amount of photometry data needed to improve the size information of km-sized TNOs.

5 Time synchronization using faint meteors

Precise time synchronization between the observation systems is essential for the coordinated occultation observations. The internal clock of the OASES control PC is thus maintained by the time information obtained with the USB GPS receiver, as described in section 3. However, the GPS time synchronization did not work perfectly in the 2016-season monitoring observations. We found that the timing of the appearances of meteors that serendipitously appeared in the observation data (see figure 12) is inconsistent between the two observation systems. The timestamps in the SER header files contain an offset from the reference time. This time offset appears to be constant (typically 1 – 5 seconds) during the turn-on of the control PC and varies randomly with observation date. The origin of the offset is thought to be imperfect time synchronization between the image capture software and the operating system of the control PC. Therefore an alternative calibration was needed for the time synchronization.

For the current dataset, we carried out an additional timing calibration using meteors that appeared in the observation data (figure 12). We developed a detection algorithm based on the meteor line detection method using the Hough Transform (Gural et al. 2008). This Python-based algorithm finds bright lines (or meteor trajectories) in a calibrated image after the subtraction and masking of stationary features such as stars (difference image; figure 12c and d, see also figure 7). The current detection algorithm is capable of detecting meteors with integrated brightness as faint as ~ 10 mag. For the timing calibration, we select meteors detected in more than two frames. With this criterion, the selected meteor should be detected as a short "line segment" in one or more frames. We thus measure the coordinates of the starting and end points of each line segment to derive the celestial coordinates of the meteor as a function of the uncalibrated time (derived from the timestamp), assuming a uniform linear motion. If there are two or more trajectories obtained in individual frames, we use the trajectory whose central position is the closest to the center of the image in the present calibration. If the integrated fluxes of the trajectories show a large variation, we use a trajectory whose integrated flux is the maximum for the calibration.

The time offset value between the two observation systems Δt is derived by minimizing da defined by the following function;

$$da = \arccos(\sin \delta_1(t_1) \sin \delta_2(t_1 + \Delta t) + \cos \delta_1(t_1) \cos \delta_2(t_1 + \Delta t) \cos(\alpha_1(t_1) - \alpha_2(t_1 + \Delta t))), \quad (14)$$

where $\alpha_i(t)$ and $\delta_i(t)$ are the right ascension and declination of the meteor observed with an observation system OASES- i at an uncalibrated time t . da thus corresponds to the average angular distance

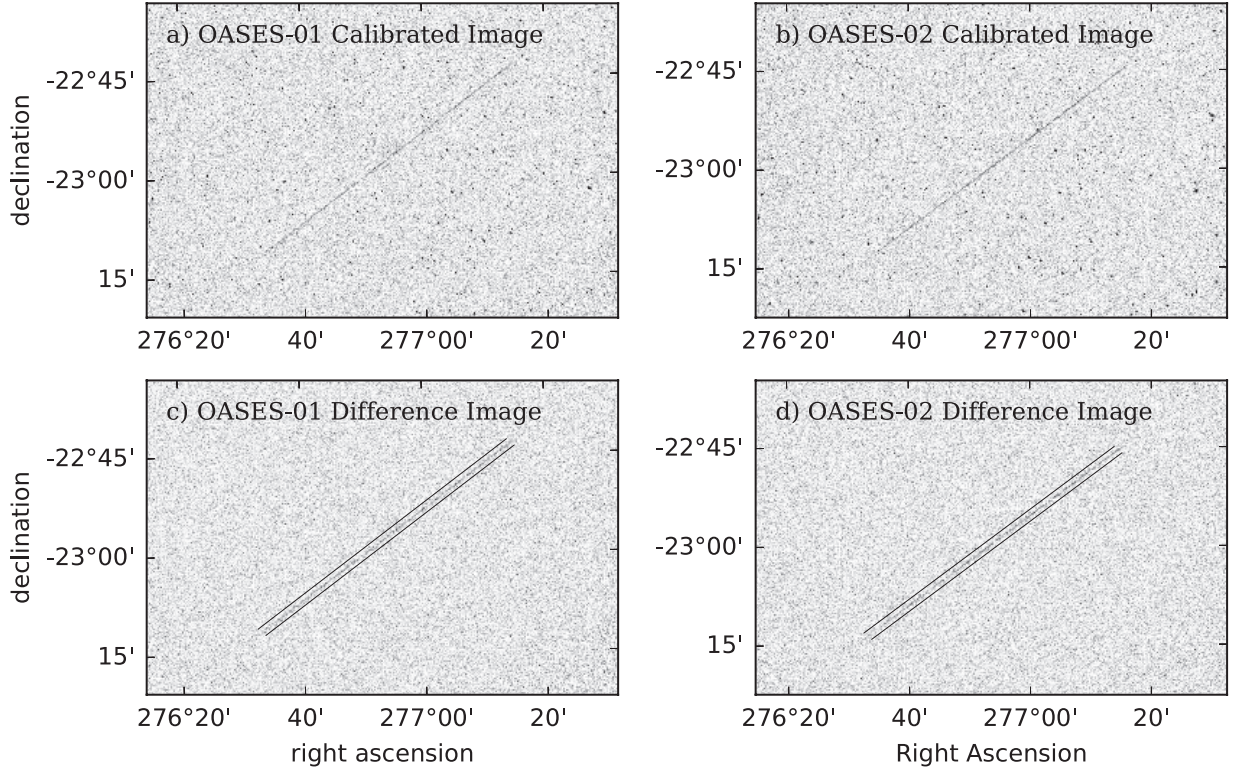


Fig. 12. Example of a faint meteor detected by the OASES monitoring observations. Panels (a) and (b) are calibrated images of the faint meteors obtained with OASES-01 and OASES-02, respectively. Panels (c) and (d) are the same as (a) and (b), but after the subtraction and masking of stationary features.

The faint meteor is highlighted by two parallel line segments.

of the same meteor observed with the two OASES observation systems (OASES-01 and OASES-02) at the uncalibrated time of t_1 and $t_1 + \Delta t$, respectively. Assuming that the parallax of the meteors can be ignored¹, the true offset Δt offers the minimum value of da . We calculate Δt for the individual meteors detected in two observation systems and adopt the average value as the offset for the time calibration.

Figure 13 shows an example of the time synchronization results. The detection rate of the meteors for the calibration is roughly ~ 5 to 10 times per one-hour observation run. After the calibration with the constant offset value, the timing between the two systems is synchronized with the 1σ accuracy of ~ 5 milliseconds, which is comparable to $1/10$ of the one-frame exposure time and is sufficient for the present study.

¹ The parallax of a meteor observed from two systems is expected to be $\sim 1'.3$ at most, assuming the altitude of the meteor is 100 km. Since the typical angular velocity of the detected meteors is $\sim 5^\circ \text{ sec}^{-1}$, the possible timing error due to the parallax is ~ 5 milliseconds at most.

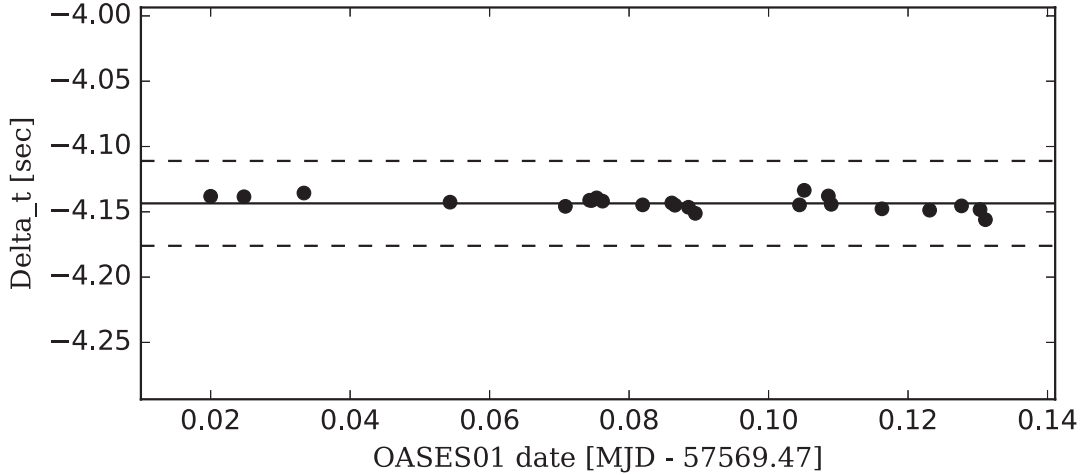


Fig. 13. Example of the time offset value Δt obtained with the time synchronization method using meteors. Filled circles represent the Δt values derived from the individual meteors. The solid line represents the average Δt value. Dashed lines correspond to the one-frame exposure time (65 millisecond), which is shown for reference. In this example, the constant offset value used for the time calibration corresponds to -4.144 seconds with a 1σ uncertainty of 0.005 seconds.

6 Summary and future prospects

We have presented an optical, high-speed, wide-field observation project, OASES, that aims to investigate stellar occultation events by km-sized TNOs. Two low-cost observation systems consisting of commercial off-the-shelf 0.28 m aperture $f/1.58$ optics and a CMOS camera were developed in OASES. The results of the monitoring observations at Miyako Islands, Okinawa, performed in 2016 demonstrate that the OASES systems are capable of high-speed (15.4 Hz cadence) simultaneous photometry of ~ 2000 stars with magnitudes down to $m_V \sim 13$, providing $\sim 20\%$ photometric precision in the light curve. We also developed a time synchronization method using faint meteors, which is needed for the simultaneous occultation detection. These developments enable us to achieve robust detection of stellar occultation events with the two independent instruments simultaneously.

This paper describes the present OASES observations for monitoring stellar occultations by TNOs. However, the OASES observation systems are capable of exploring other rare and short-timescale astronomical events, such as faint meteors, lunar impact flashes, near-Earth asteroids and space debris. In fact, dozens of faint meteors are detected in one night of OASES observations simultaneously (see section 5). Since these astronomical events are rare and non-repeatable, simultaneous detection with multiple instruments is essential for their statistical analysis. Thanks to the unique capability of wide-field high-cadence imaging and the cost-effectiveness of the OASES observation systems, OASES will be key instruments for pioneering observations in high time resolution astronomy.

As of 2017, the OASES project has developed two observation systems. A primary mon-

itoring observation campaign with the two systems began in June 2016 and is now underway. We plan to continue the observation campaign with the two systems until 2018. However, unlike other observation programs, the number of observation systems can be easily increased because of their low cost. As noted in previous studies (Lehner et al. 2010), adding systems significantly reduces the false-positive detection rate. Therefore the OASES observations will be capable of achieving more robust detection of occultations when additional systems are installed. This upgrade is currently in its conceptual design phase. We also note that the instruments used for the present OASES observation system are easily available for amateur astronomers. The present observation project thus demonstrates an opportunity for them to participate in cutting-edge astronomical studies.

We thank the personnels of Miyakojima City Museum and of Miyako open-air school (*Miyako Seishonen no Ie*) for cooperating on the OASES observations at Miyako Island. We also thank the people of the in Miyako Island for supporting our observations. This research has been partly supported by JSPS grants (JP26247074, 15J10278, 26800112, and 16K17796).

References

- Berry R & Celestron Engineering Team 2016, *The Story of the Rowe-Ackermann Schmidt Astrograph Version 01*, Celestron, LLC.,
http://www.celestron.com/media/1214965/rasa_white_paper_low_res.pdf
- Bianco, F. B., et al. 2010, *AJ*, 139, 1499
- Chiang, E., & Youdin, A. N. 2010, *Annual Review of Earth and Planetary Sciences*, 38, 493.
- Duncan, M. J., & Levison, H. F. 1997, *Science*, 276, 1670
- Elliot, J. L. et al. 2005, *AJ*, 129, 1117
- Fraser, W. C. & Kavelaars, J. J. 2008, *Icarus* 198, 452
- Greenstreet, S., Gladman, B., & McKinnon, W., B. 2015, *Icarus* 258, 267
- Gural, P. S. 2008, *Earth Moon Planets*, 102, 269
- Harding, L. K., et al. 2016, *MNRAS*, 457, 3036
- Jewitt D., Luu J. 1993, *Nature*, 362, 730
- Kamata, Y. et al. 2004, *SPIE*, 5499, 210
- Lang, D., Hogg, D. W., Mierle, K., Blanton, M., & Roweis, S., 2010, *AJ*, 139, 1782
- Lasker, B. B., et al. 2008, *AJ*, 136, 735
- Lehner, M. J. et al. 2009, *PASP*, 121, 138
- Lehner, M. J. et al. 2010, *PASP*, 122, 959
- Lehner, M. J., et al. 2014, *SPIE*, 9145, 13

- Liu, C.-Y., Doressoundiram, A., Roques, F., Chang, H.-K., Maquet, L., & Auvergne, M. 2015, MNRAS, 446, 932
- Nihei, T. C., Lehner, M. J., Bianco, F. B., King, S.-K., Giammarco, J. M., & Alcock, C. 2007, AJ, 134, 1596
- Oort, J. H. 1950, Bull. Astron. Inst. Neth. 11, 91
- Schlichting, H. E., Ofek, E. O., Wenz, M., et al. 2009, Nature, 462, 895
- Schlichting, H. E., Fuentes, C. I., & Trilling, D. E. 2013, AJ, 146, 36
- Stern S. A. et al. 2015, Science, 50, 292
- Volk, K., & Malhotra, R. 2008, ApJ, 687, 714
- Zhang, Z.-W., et al. 2009, PASP, 121, 1429
- Zhang, Z.-W., Lehner, M. J., Wang, J.-H., et al. 2013, AJ, 146, 14